

Pulsation Mechanisms

Michael Scholz

University of Heidelberg

$$\frac{\partial M_{r_0}}{\partial r_0} = 4\pi r_0^2 s_0$$

$$\frac{\partial M_r}{\partial r} = 4\pi r^2 s$$

$$\frac{\partial p_0}{\partial r_0} = -s_0 \cdot \frac{GM}{r_0^2} r_0$$

$$\frac{\partial p}{\partial r} = -s \cdot \left(\frac{GM}{r^2} + \frac{\partial^2 r}{\partial t^2} \right)$$

$$p = p_g + p_{\text{rad}} + \dots \approx \mathcal{R} T s / \bar{\mu} + 4\sigma_{\text{SB}} T^4 / 3c + \dots$$

$$M_r(t, r_0) = M_{r_0}(r_0)$$

$$r(t, r_0) = r_0 (1 + \xi(t, r_0))$$

$$s(t, r_0) = s_0(r_0) (1 + \eta(t, r_0))$$

$$p(t, r_0) = p_0(r_0) (1 + \xi(t, r_0))$$

$$\xi, \eta, \xi \ll 1$$

$$\frac{s_0}{p_0} \left[\frac{\partial^2 \xi}{\partial t^2} - \frac{GM}{r_0^3} r_0 (4\xi + \xi) \right] + \frac{1}{r_0} (1 + 2\xi) \frac{\partial \xi}{\partial r_0} = 0$$

$$(p/p_0) = (s/s_0)^{\Gamma_1}$$

$$\left. \frac{d \ln p}{d \ln s} \right|_{\text{ad}} = \Gamma_1; \quad \left. \frac{d \ln p}{d \ln T} \right|_{\text{ad}} = \frac{\Gamma_2}{\Gamma_2 - 1}; \quad \left. \frac{d \ln T}{d \ln s} \right|_{\text{ad}} = \Gamma_3 - 1; \quad \frac{\Gamma_2}{\Gamma_2 - 1} = \frac{\Gamma_1}{\Gamma_3 - 1}$$

$$\frac{s_0}{p_0} \left[\frac{\partial^2 \xi}{\partial t^2} - \frac{GM}{r_0^3} \left\{ (4 - 3\Gamma_1) \xi - \Gamma_1 r_0 \frac{d\xi}{dr_0} \right\} \right] + \frac{1}{r_0} (1 + 2\xi) \frac{\partial \xi}{\partial r_0} = 0$$

negligible $\partial \xi / \partial r_0$ and $\partial \xi / \partial r_0$ terms near $r_0 = R_0$

$$\frac{\partial^2 \xi}{\partial t^2} + \frac{GM}{R^3} (3\Gamma_1 - 4) \xi = 0$$

$$\ddot{\xi} + \omega^2 \xi = 0$$

$$\begin{aligned} \rho &= 2\pi / \omega = 2\pi M^{-1/2} R^{3/2} [G(3\Gamma_1 - 4)]^{-1/2} \\ &= 2\pi \bar{s}^{-1/2} [4\pi G(3\Gamma_1 - 4)/3]^{-1/2} \\ &= 2\pi \tau_{\text{hyd}} [3\Gamma_1 - 4]^{-1/2} \\ &= 2\pi L^{3/4} M^{-1/2} T_{\text{eff}}^{-3} [G(3\Gamma_1 - 4)(4\pi \epsilon_{\text{SB}})^{3/2}]^{-1/2} \end{aligned}$$

$$Q = \rho \cdot \sqrt{\bar{s}/\epsilon_0} = 0.116 d / \sqrt{3\Gamma_1 - 4}$$

$$\xi(t, r_0) = \tilde{\xi}(r_0) e^{i\omega t}; \quad \eta(t, r_0) = \dots; \quad \zeta(t, r_0) = \dots$$

$$\frac{\partial^2 \tilde{\xi}}{\partial r_0^2} + \left(\frac{4}{r_0} - \frac{s_0 g_0}{\rho_0} \right) \frac{\partial \tilde{\xi}}{\partial r_0} + \frac{s_0}{\Gamma_1 \rho_0} \left(\omega^2 + (4 - 3\Gamma_1) \frac{g_0}{r_0} \right) \tilde{\xi} = 0$$

$$g_0 = G M_{r_0} / r_0^2$$

$$\tilde{\xi} = 0 \quad \text{at} \quad r_0 = 0$$

boundary conditions:

$$\text{center} : \partial \tilde{\xi} / \partial r_0 = 0$$

$$\text{"surface"} : \rho = \dots, \text{ e.g. } 4\pi R^2 \rho = G M_{\text{atm}} M / R^2$$

$$\longrightarrow \Gamma_1 R_0 \partial \tilde{\xi} / \partial r_0 - (4 - 3\Gamma_1) \tilde{\xi} = 0$$

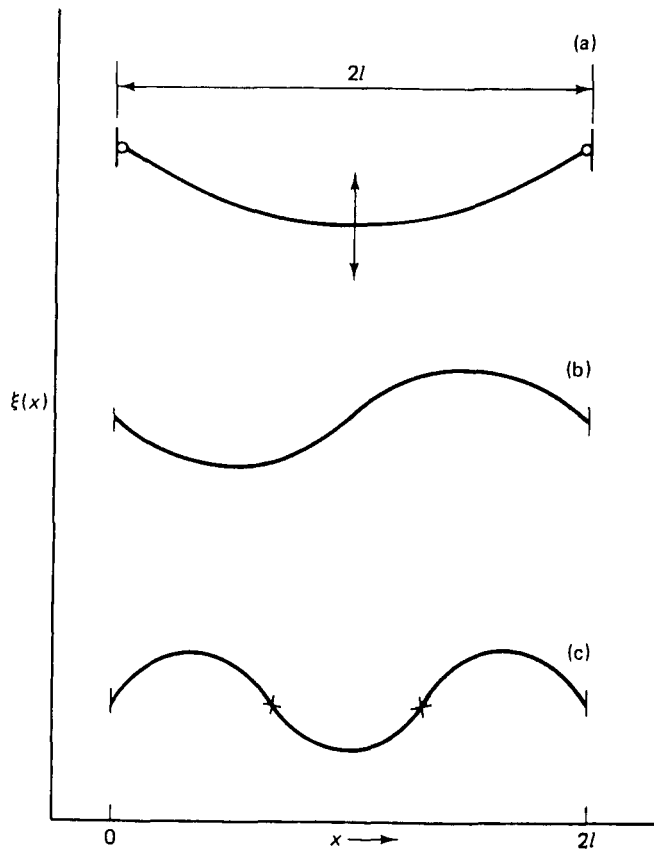


Fig. 18.1. (a) A rope of length $2l$ is fastened at both ends. It is free to oscillate in the center. It has a fundamental frequency ν_0 for a standing wave with nodes only on both ends. (b) The first overtone with frequency ν_1 for standing waves has a node in the center of the rope and the maximum amplitude at distance $d = \frac{1}{2}l$ from the walls. (c) The second overtone mode for standing waves has two nodes at distance $d = \frac{2}{3}l$ from the walls and maximum amplitude in the center and at distance $d = \frac{1}{3}l$ from the walls.

Böhm-Vitense 1992, Introduction to Stellar Astrophysics III

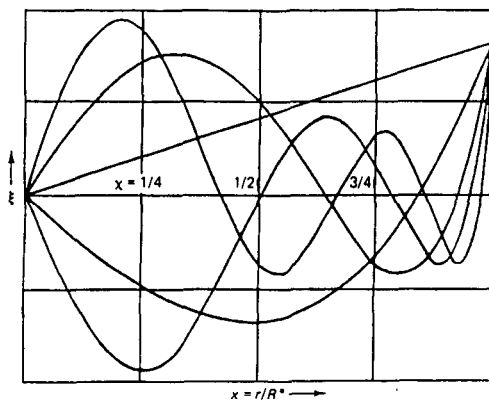


Fig. 18.2. The eigenfunctions $\xi_i(x)$ are shown as calculated for a (hypothetical) homogeneous density star. The amplitudes must be zero at the center. From Rosseland (1949).

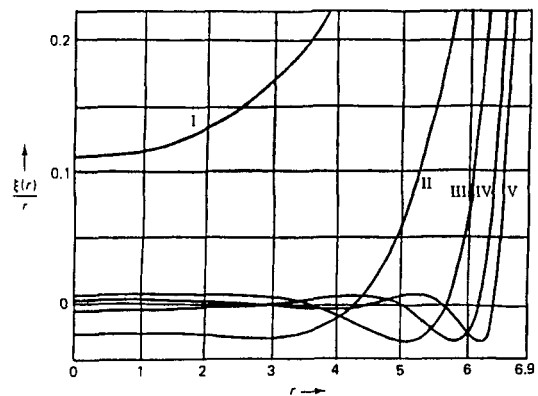


Fig. 18.3. The eigenfunctions $\xi_i(r)/r$ are shown for a star whose temperature and density stratification follow a polytrope with index $n = 3$. For the larger central density, as compared to the homogeneous star, the amplitudes in the center decrease strongly. The index of the harmonics is given in roman numerals. I indicates the fundamental mode. II the first harmonic etc. From Rosseland (1949). $\rho = \rho_g \cdot \Gamma_1 = 5/3$.

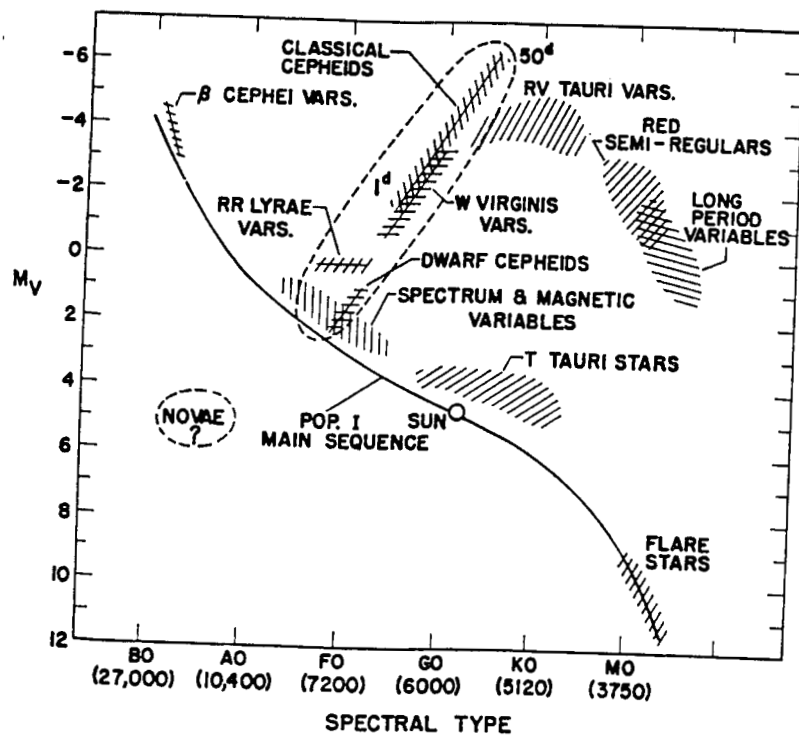


Fig. 27.1 Location of various types of intrinsic variables on the Hertzsprung-Russell diagram.
Cox & Giuli 1968, Principles of Stellar Structure II

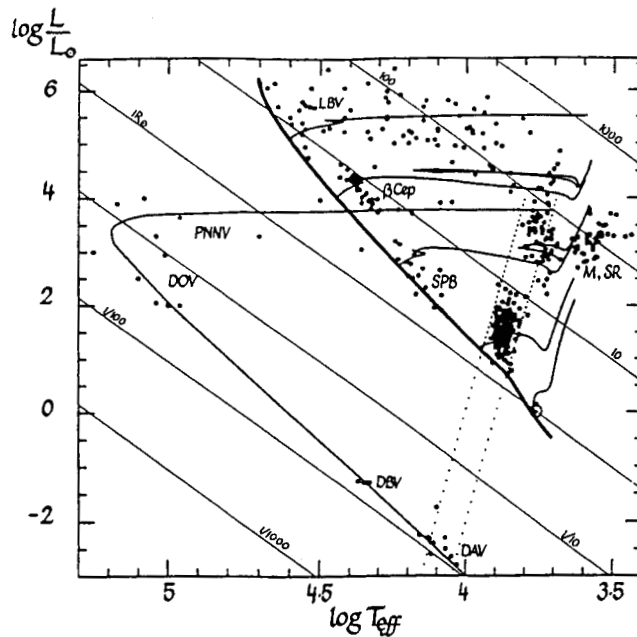


Figure 1. Distribution of some observed pulsating variable stars (dots) on the HR diagram. For convenience some guiding lines from stellar evolution are included. The heavy line passing from upper left to lower right shows the ZAMS. Evolutionary paths for some stellar masses, labeled at the tracks, are included. Common abbreviations are added to the figure indicating the location of some major families pulsating variable stars.

Gautschi 1995, in: Stohr & Whitelock (eds) Astrophysical
Evolution of Stellar Pulsation, 1995, p. 155, p. 31

$$L_r = 4\pi r^2 (\phi_{\text{rad}} + \phi_{\text{conv}} + \dots)$$

$$\phi_{\text{rad}} = - \frac{16\sigma_{\text{SB}} T^3}{3k_{\text{Ross}} g} \frac{dT}{dr} = -4\pi r^2 \frac{16\sigma_{\text{SB}} T^4}{3k_{\text{Ross}}} \frac{d \ln T}{dM_r}$$

Fig. 1. Schematic drawing of the transition region.
Adapted from Osaki (1982).

———— SURFACE

FLUX VARIATIONS
"FROZEN-IN;" VERY
NON-ADIABATIC

} NO DRIVING } thickness roughly given by:
total internal energy
~ $L_0 \cdot P$

////// TRANSITION REGION

QUASI-ADIABATIC } NO NET DRIVING

↑↑ RADIATIVE FLUX

Cox 1985, in: Madore (ed) Cepheids: Theory and Observations,
IAU coll. 82, p. 126

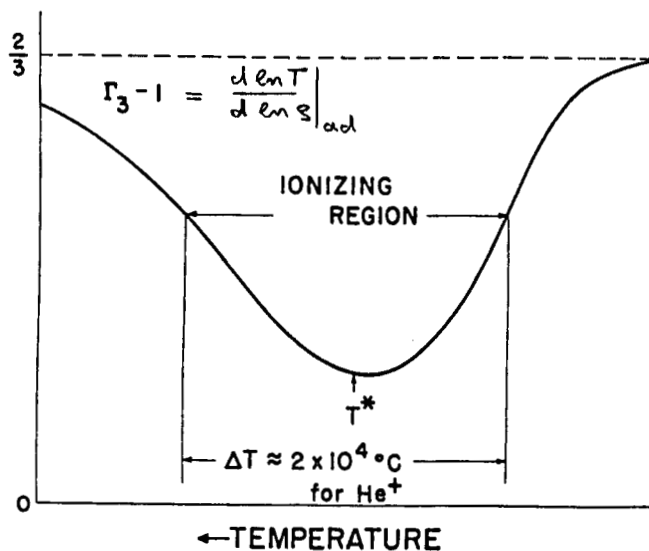


Fig. 27.4 $\Gamma_3 - 1$ vs. temperature (schematic) in the region of He^+ ionization in the equilibrium model of a stellar envelope.

Cox & Giuli 1968, Principles of Stellar Structure II

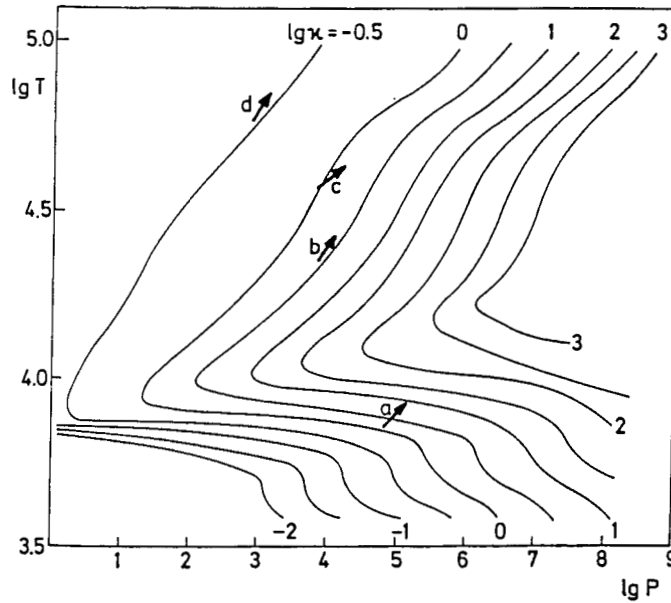


Fig. 39.1. Lines of constant opacity κ in the $\lg P$ - $\lg T$ plane (all values in cgs). Four arrows are shown that indicate the direction in which a mass element moves during adiabatic compression. For the arrows labelled a , b , and d the direction is given by $\nabla_{ad} = 0.4$. In case a the arrow points in the direction of increasing κ , i.e. the κ mechanism has a "driving" effect on pulsations. In cases b and d the arrows point in the direction of decreasing κ , indicating a "damping" (or almost neutral) effect on pulsation. In case c the direction of the arrow is different from that of the other ones, since ∇_{ad} is here reduced by the second ionization of helium. Because of this reduction, the arrow points in the direction of increasing κ and this ionization region can contribute considerably to the excitation of pulsations in Cepheids

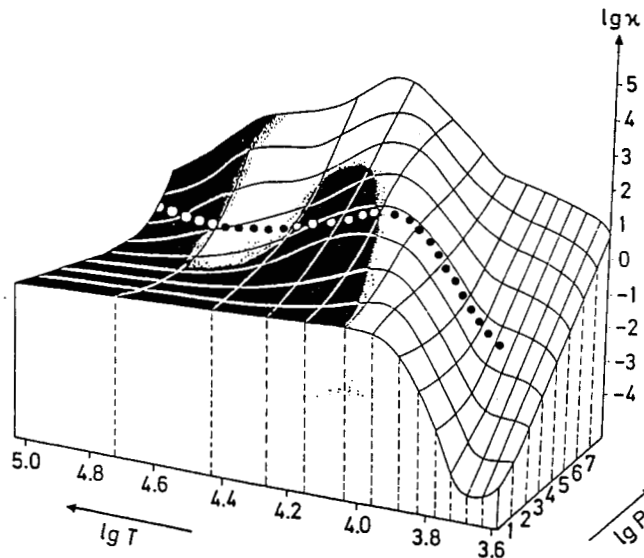


Fig. 39.2. An opacity surface (" κ mountain") for the outer layers of a star as in Fig. 17.5. But this time the dependence with respect to P (in dyn cm^{-2}) and T (in K) is shown. The dotted line corresponds to the stratification inside a Cepheid of $7M_{\odot}$. The white areas of the "mountain" indicate regions which excite the pulsation, the black ones those which damp it. The excitation in the region of $\lg T \approx 4.6$ is due to the second ionization of helium

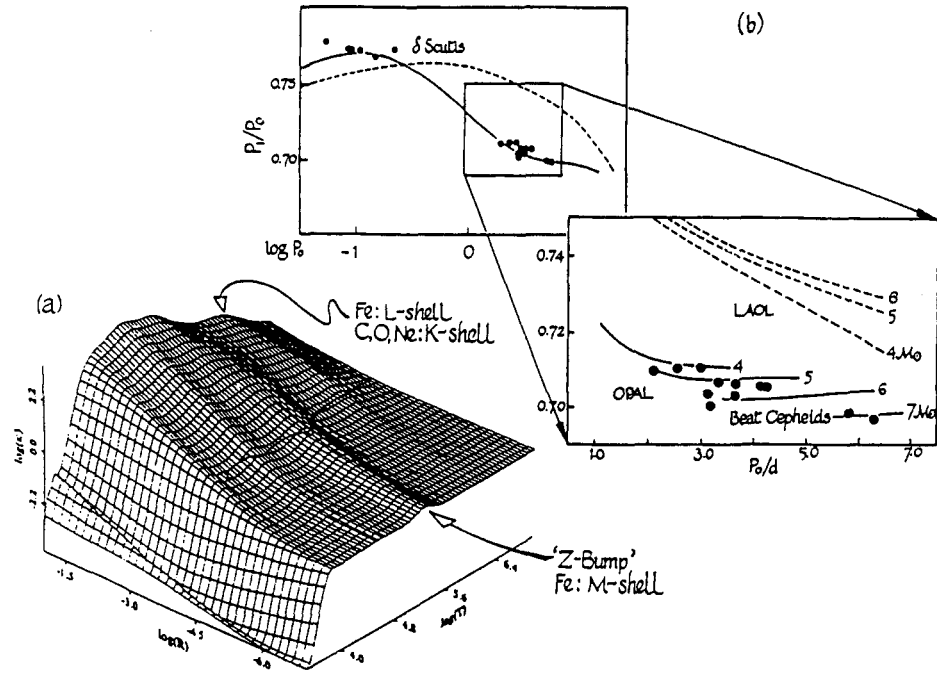


Figure 2. (a) The "opacity mountain" as obtained from OP calculations for a $X = 0.7$, $Z = 0.02$ composition. The two most prominent new features (ridges) found in the new opacity data are indicated. The solid line meandering along the slope of the κ -mountain marks the path traced out by the interior of a $12M_\odot$ ZAMS model. (b) Petersen diagram (P_1/P_0 vs. P_0) for population I variables (δ Sct and double-mode Cepheids). Dots indicate observed period data. Dashed lines clearly display the disagreement with the old LAOL data. Solid lines show the results of Moskalik et al. (1992) (lower right) and of Christensen-Dalsgaard (1993) (upper left), both based on OPAL opacity data. Gautschi 1995, in: Stobie & Whitelock (eds) *Astrophysical Applications of Stellar Pulsation*, IAU Coll. 155, p. 31

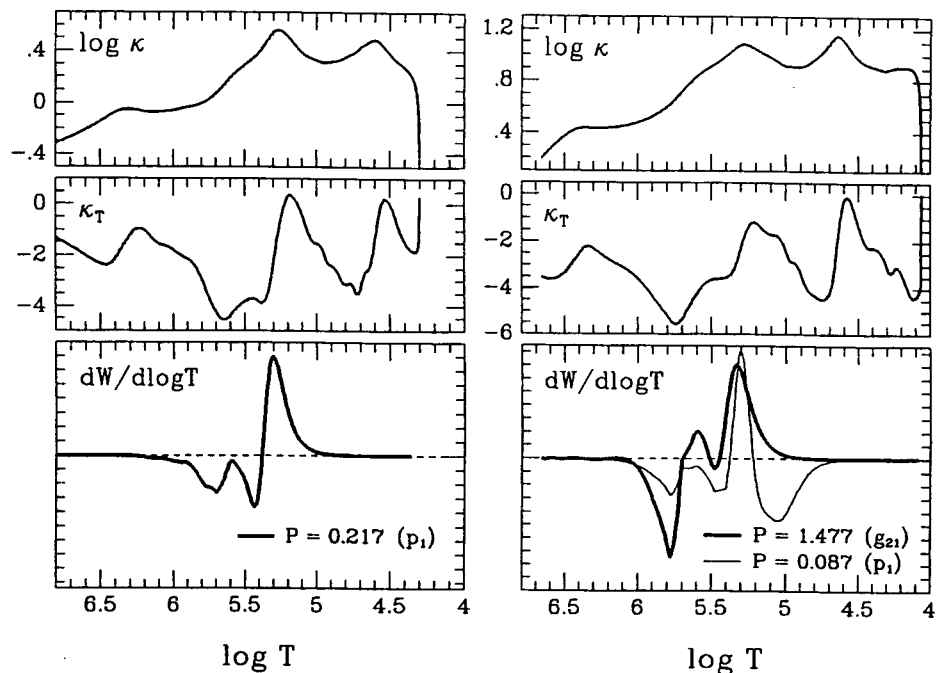
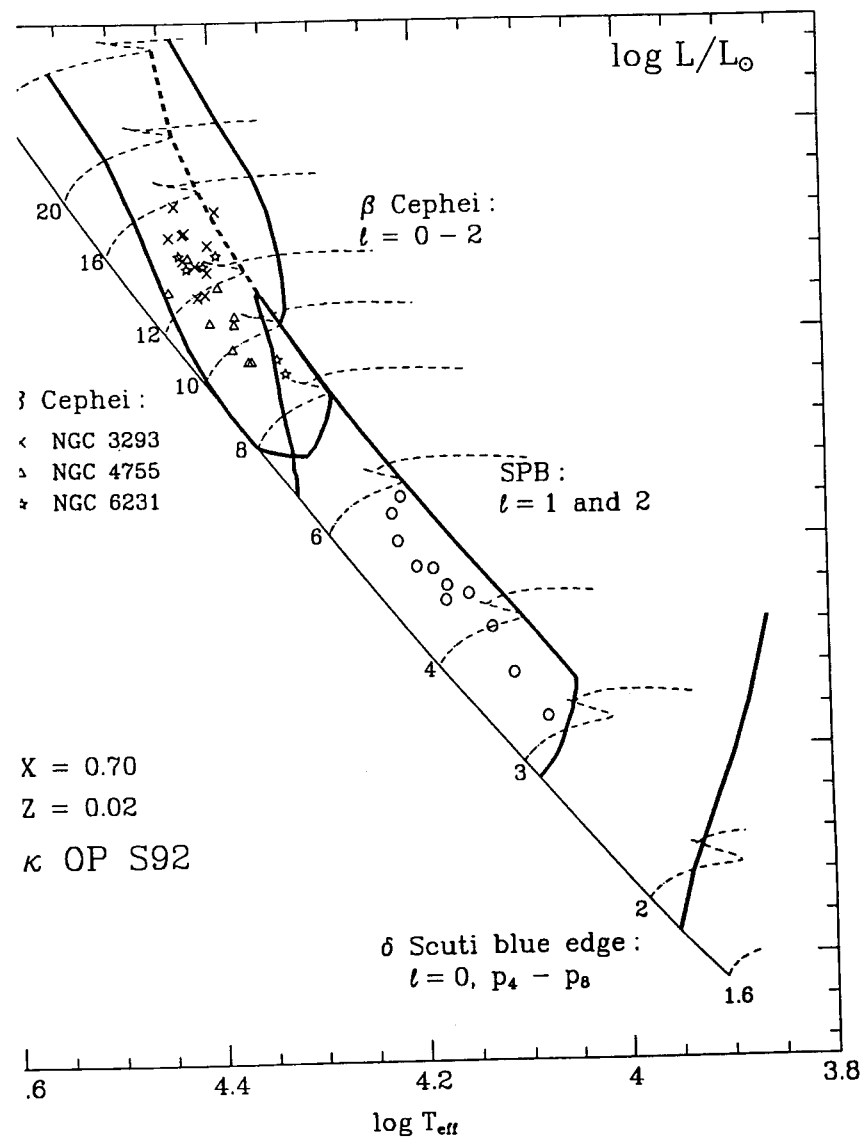


Figure 1. Theoretical instability domains of the β Cep and the Slowly Pulsating B-type Stars in the H-R diagram. Only modes of $\ell \leq 2$ are considered. The models are computed with OP tables (S92 mixture, see Seaton et al. 1994) for standard composition of $X = 0.7$, $Z = 0.02$. For comparison we show β Cep stars observed in young open clusters NGC 3293, NGC 4755 and NGC 6231 (Balona 1994; Balona & Koen 1994; Heynderickx 1991) and the field SPB stars (Waelkens 1994). From Pamyatnykh et al. (in preparation).

Figure 2. Opacity κ , opacity derivative κ_T , and differential work integral $dW/d\log T$ (positive in driving zone) for selected pulsation models, plotted vs. temperature. Left: β Cep star model ($M = 12M_\odot$, $\log L/L_\odot = 4.27$, $\log T_{\text{eff}} = 4.378$, $X_c = 0.13$). Right: SPB-star model ($M = 4M_\odot$, $\log L/L_\odot = 2.51$, $\log T_{\text{eff}} = 4.142$, $X_c = 0.37$). Both models have initial composition of $X = 0.7$, $Z = 0.02$. The modes plotted correspond to $\ell = 1$.

Moskalik 1995, in: Stobie & Whitelock (eds) *Astrophysical Applications of Stellar Pulsation*, IAU Coll. 155, p. 44

Moskalik 1995, in: Stobie & Whitelock (eds) *Astrophysical Applications of Stellar Pulsation*, IAU Coll. 155, p. 44

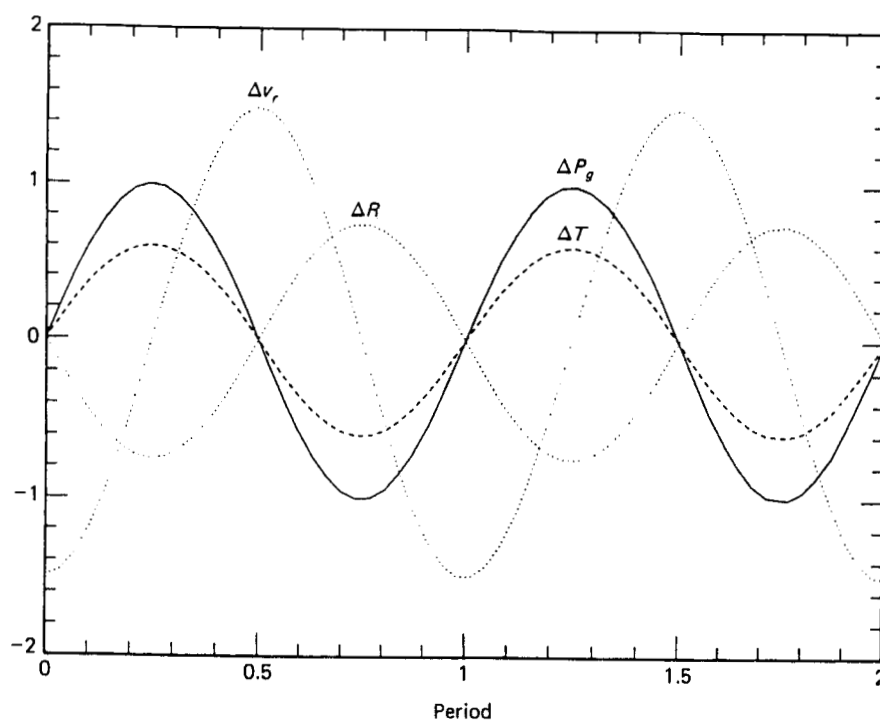


Fig. 18.5. The velocity, radius, pressure and temperature variations for adiabatic pulsations are shown schematically. Pressure and temperature are highest for the smallest radius. For excess pressure, the layers are accelerated outwards. For decreased pressure, gravity pulls inwards. Arbitrary units.

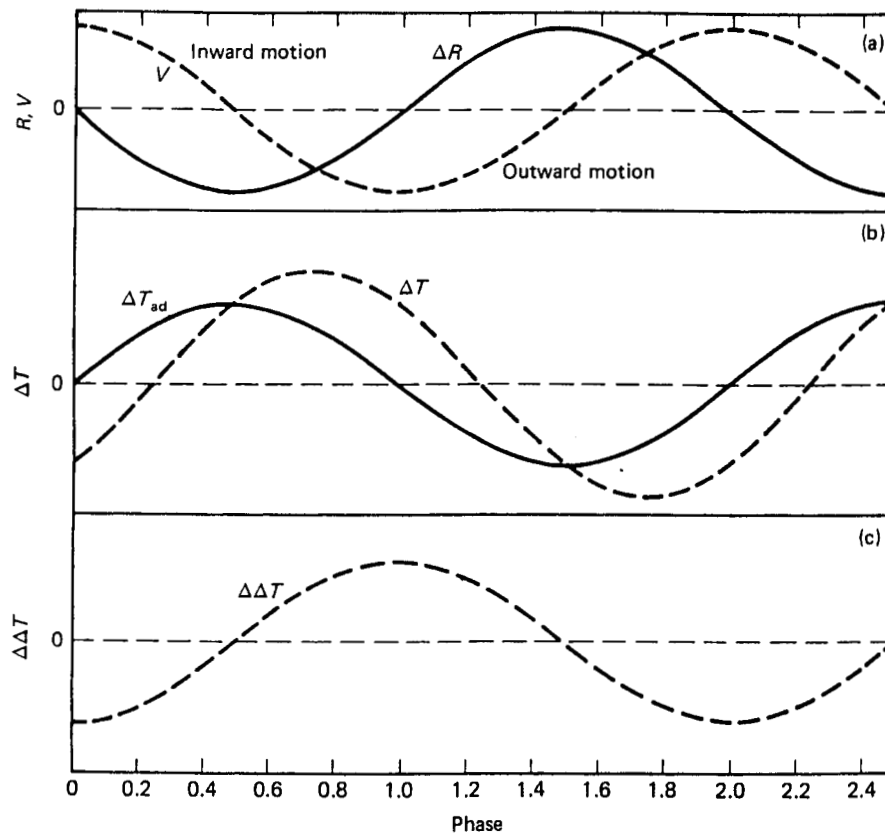


Fig. 18.8. (a) Adiabatic radius and velocity variations as a function of phase for a Cepheid (arbitrary scale). Negative velocities mean outward motion, positive velocities falling motion. (b) The adiabatic temperature variations ΔT_{ad} (solid line). Maximum ΔT_{ad} occurs for minimum radius, and vice versa. In those layers where κ is increasing with increasing T and P_g , excess heating occurs during phases of positive ΔT and ΔP_g . (Excess cooling occurs for negative ΔT and ΔP_g .) (c) The excess temperature increase, $\Delta\Delta T$ is shown schematically. It increases throughout the phase of positive ΔT and ΔP_g . Only after expansion has proceeded beyond the equilibrium radius does $\Delta\Delta T$ actually decrease. In (b) the final $\Delta T = \Delta T_{ad} + \Delta\Delta T$ is shown schematically as a function of time (dashed line). $\Delta P_g \propto \Delta T$ is larger during expansion phases than during contraction

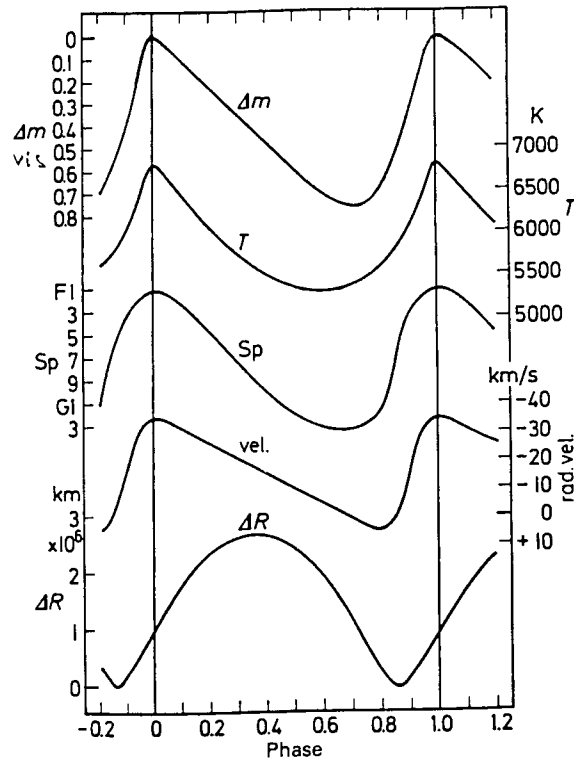


Fig. 16.4. The observed variations of the apparent visual magnitudes, the effective temperatures, the spectral types, and the radial velocities for δ Cephei are shown as functions of phase. At the bottom the changes in the radius are shown, which can be obtained by integrating over the pulsational radial velocities (the stellar velocity has to be subtracted from the observed velocities). It can be seen that the radius is nearly the same for maximum and minimum brightness. (From W. Becker 1950.)

Böhm-Vitense 1989, Introduction to Stellar Astrophysics I

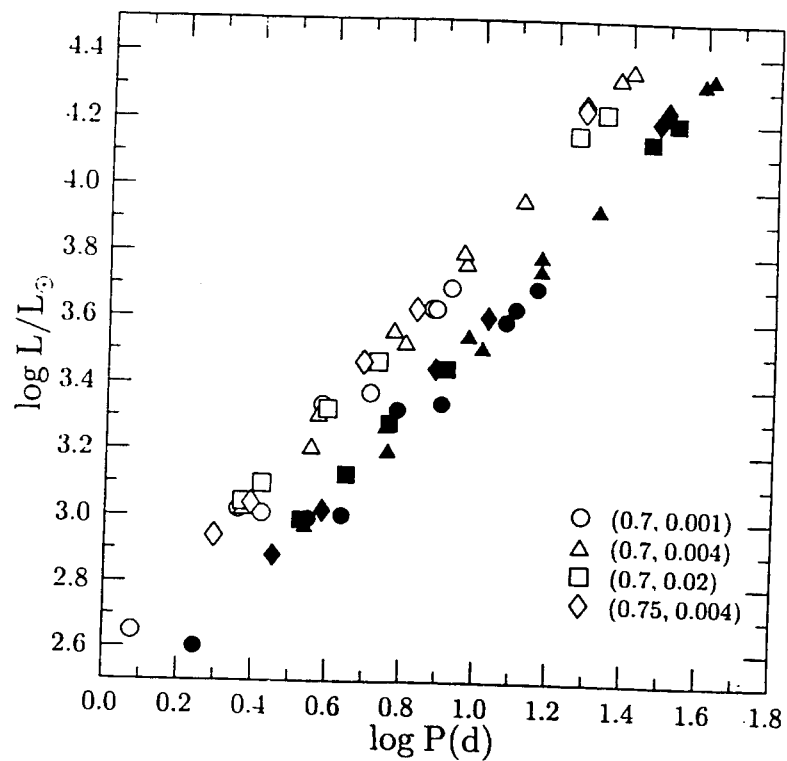


FIG. 2.—Period-luminosity relation for the blue edge (*open symbols*) and for the ad hoc defined red line (*filled symbols*). All different chemical compositions are shown in the same graph. model study
Saio & Gantichy 1998, A&A 418, 360

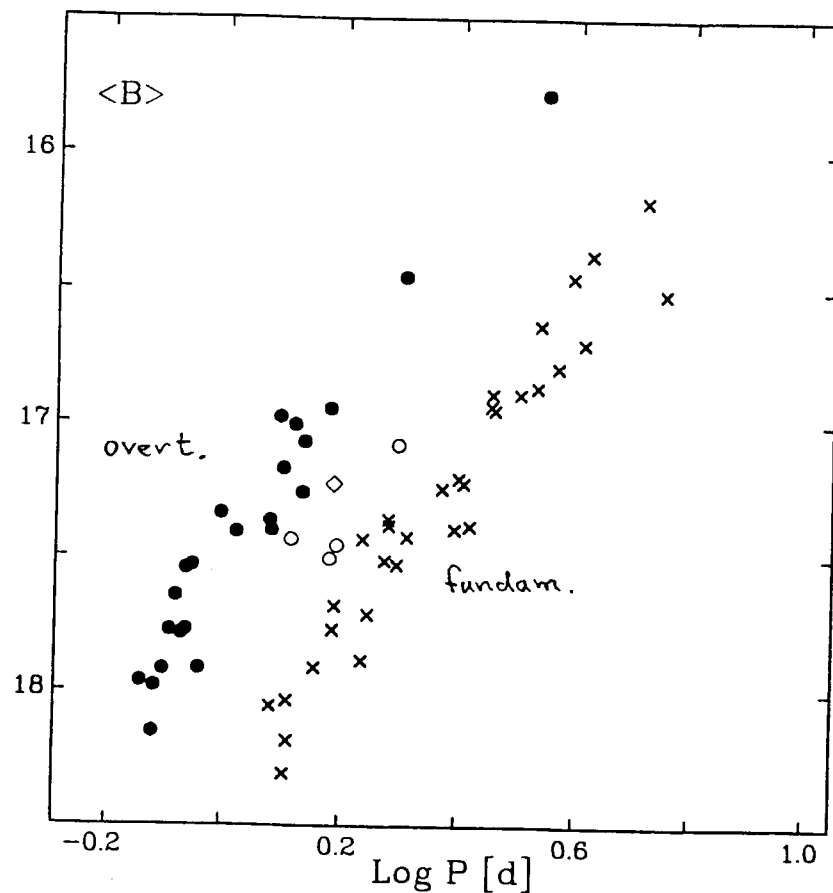
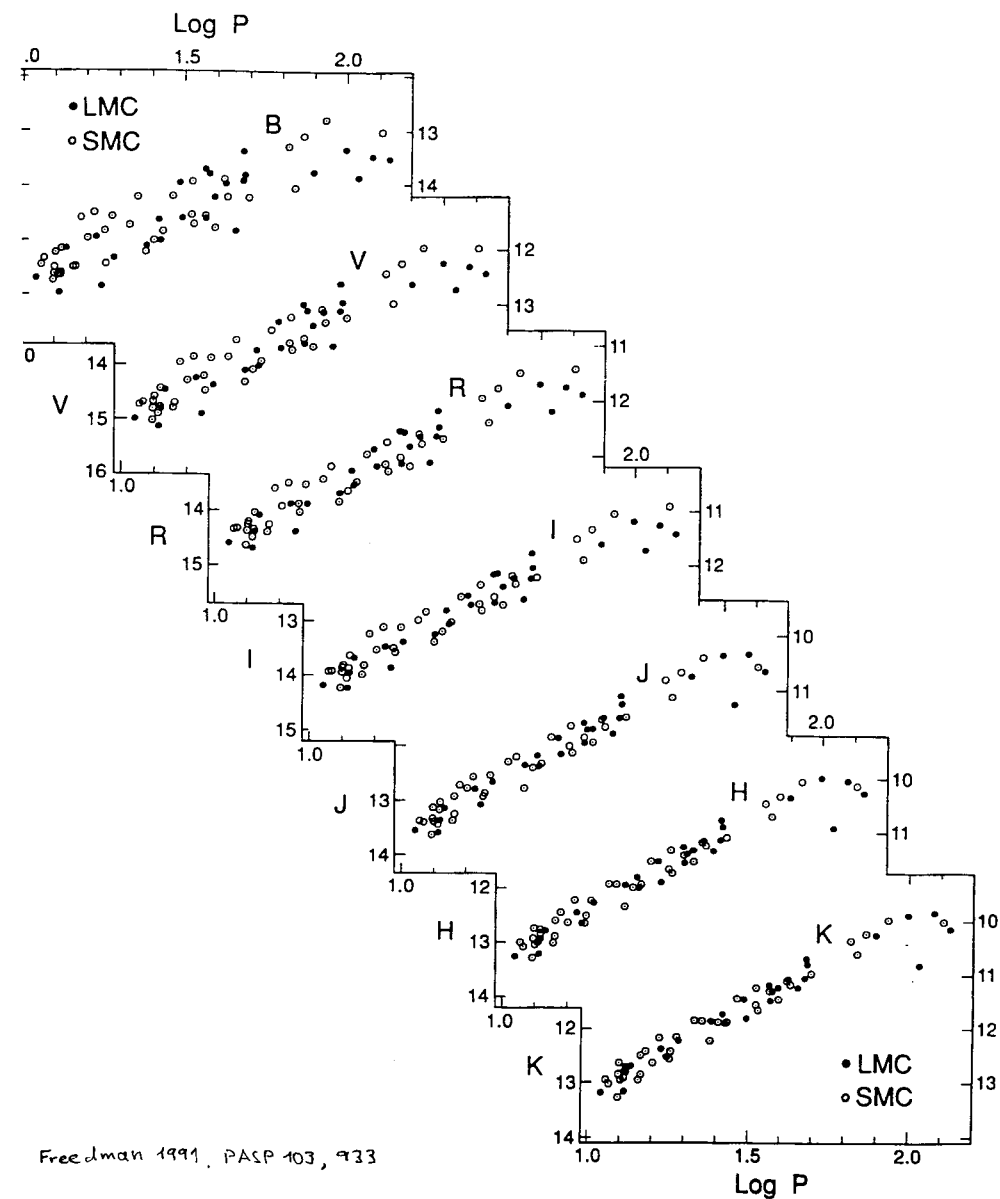


Fig. 1. Period-luminosity relation for the edited sample of SMC Cepheids Fourier analysis
Buchler & Moskalik 1994, A&A 292, 450

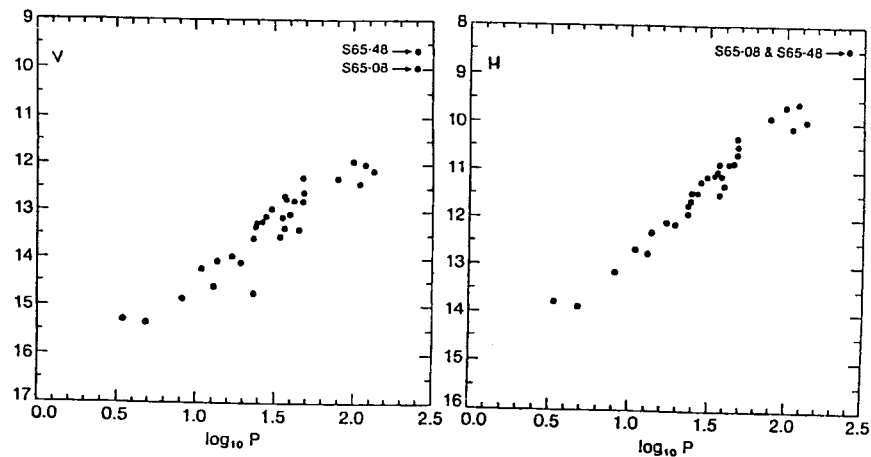


Freedman 1991, PASP 103, 933

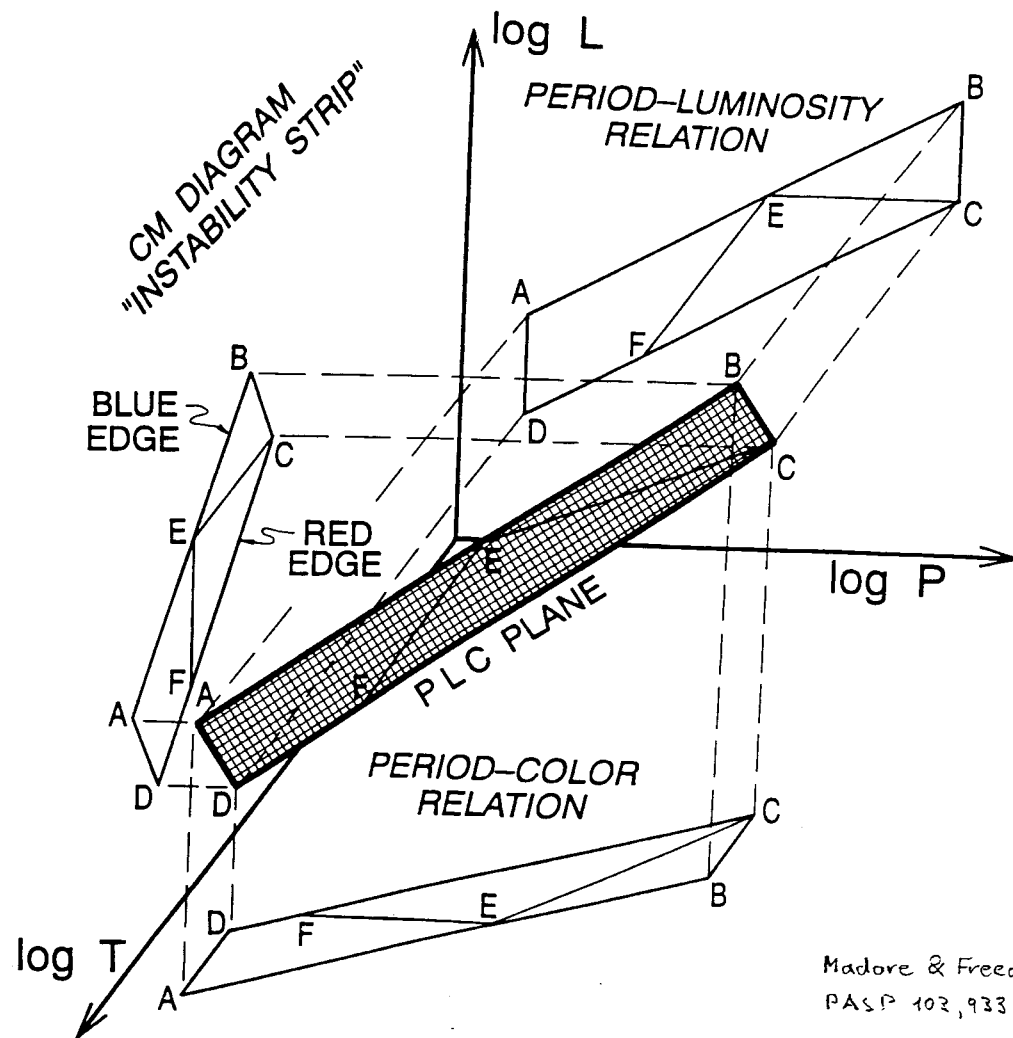
LMC Cepheid period-luminosity relations at seven wavelengths, from the blue to the near-infrared, constructed from a data set (Freedman & Madore 1992). LMC Cepheids are shown as filled circles; SMC data, shifted to the LMC modulus, are shown as

Fig. 1. The $\langle V \rangle$ Period-Luminosity relation for 33 LMC Cepheids for which both V and H observations are available.

Fig. 2. The $\langle H \rangle$ Period-Luminosity relation for 33 LMC Cepheids, including the two new Leavitt variables at 250 days.



Grievé et al 1985, in: Madore (ed) Cepheids: Theory and Observations, IAU Coll. 82, p. 215



Madore & Freedman 1991,
PASP 103, 933

FIG. 3—The Cepheid Manifold: Projections of the PLC plane (shown shaded) onto the three principal coordinate systems (luminosity [$\log L$] increasing up, period [$\log P$] increasing to the right, and color [$\log T$] becoming bluer/hotter to the lower left). The backward projection onto the ($\log L$, $\log P$) plane gives the period-luminosity relation. Projecting to the left gives the position of the instability strip within the color-magnitude diagram. Projecting down gives the period-color relation. EC is a line of constant luminosity. EF is a line of constant color. AD and BC are lines of constant period.

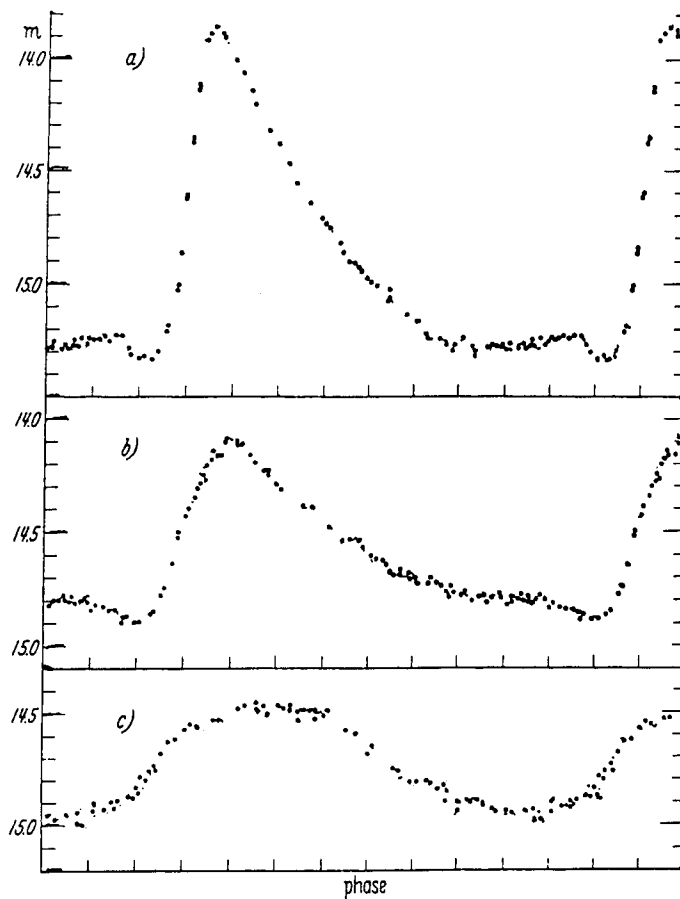


Fig. 16.5. The light curves for the three Bailey types of RR Lyrae stars are shown. Types *a* and *b* only differ in amplitude. The *c* RR Lyraes show a nearly sinusoidal light variation. (From Ledoux & Walraven 1958.)

Röhm-Vitense 1929, Introduction to Stellar Astrophysics I

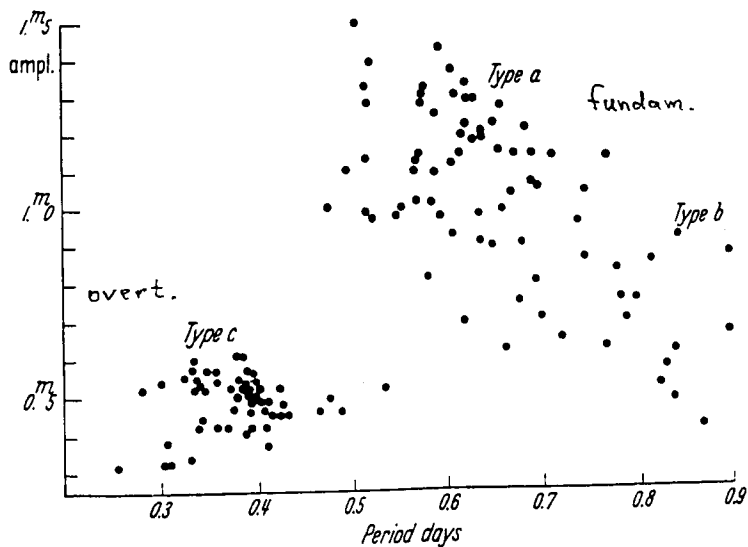


Fig. 16.6. We show the relation between amplitude and period for the three types of RR Lyrae stars. The *c* types have the shortest periods and the lowest amplitudes. They are clearly distinct from the *a* and *b* types. (From Ledoux & Walraven 1958.)

Alvarez et al 1997, A&A 327, 656

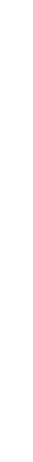


Fig. 3. Period-luminosity relations in K band. Crosses represent Miras belonging to group 1, triangles to group 2 and squares to group 3. Solid line and dashed line are the PL fit relations for group 1 and 3 respectively. Solid line is the PL relation determined by van Leeuwen (1997)

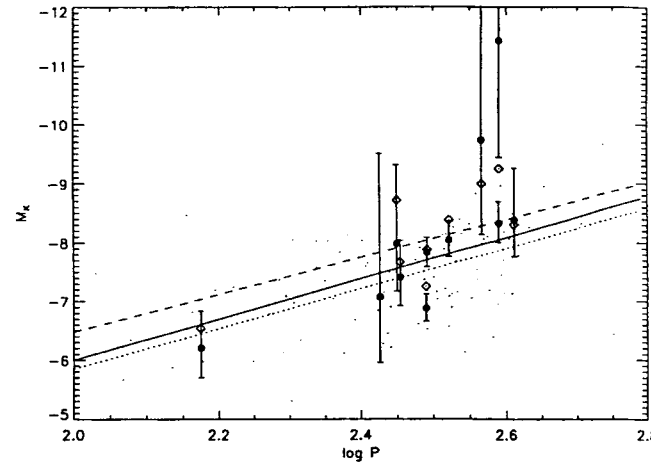


Fig. 5. Period-luminosity relations in K band. The lines have the same meaning as in Fig. 3. Filled circles are the Miras used by van Leeuwen et al. (1997) to calibrate the zero-point of the Galactic PL relation and diamonds are their M_K value as determined by the LM method when available. The other sample stars are represented by dots



Fig. 4. Same as Fig. 1 but with the FGWC89 data.

Gautschy 1999, A&A 349, 209



Fig. 6. Same as Fig. 1 for the Galactic data of RF81 and vL97.



Fig. 1. PL data of HW90 observations and results from radial pulsation computations. F-mode data for each mass choice is plotted as a line. The lowest line results from the $0.8 M_{\odot}$ models. The masses 5, 2.0, 3.0, 4.0, and $5.0 M_{\odot}$ follow towards higher luminosities. The same ordering applies to O1 results displayed with dashed lines.

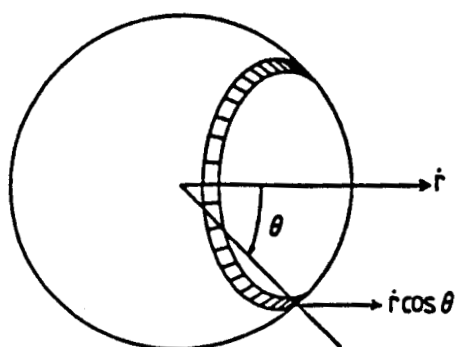


Fig. 13 Geometrical projection of stellar velocity fields

Gautschy 1987, *Vistas Astron.* 30, 197

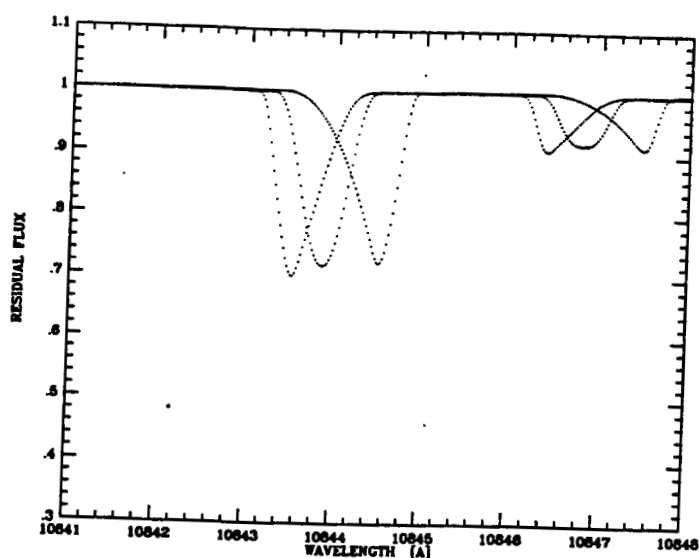


FIG. 3.—Line profile changes due to radial pulsation of the photosphere. They are illustrated for three different pulsation velocities of a model atmosphere with $T_{\text{eff}} = 5500$ K and $\log g = 1.5$. The velocities from left to right are -10 , 0 , and $+20$ km s $^{-1}$, respectively. The two spectral lines in this excerpt from the spectrum synthesis are Si I and Ca I. Sasselov & Lester 1990 ApJ 362, 333 CS models

The Baade-Wesselink Method
Gautschi 1987, Vistas Astron. 30, 197

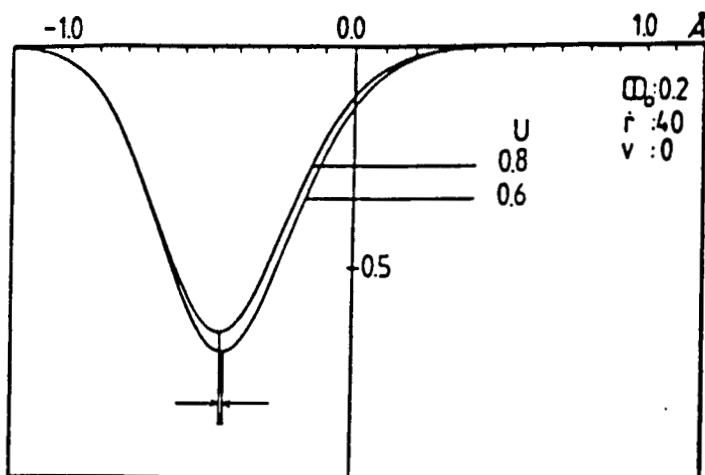


Fig. 14

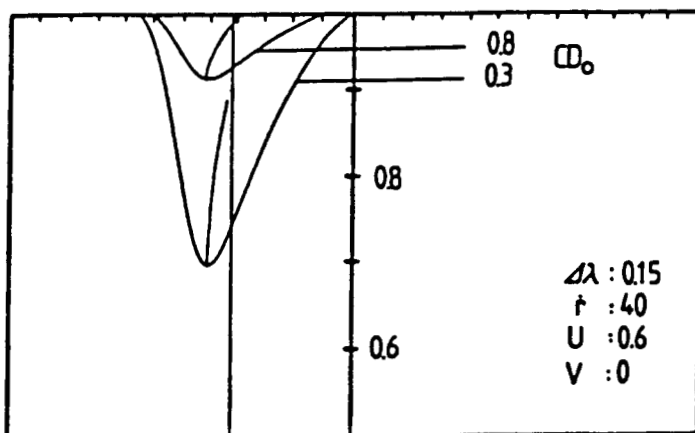


Fig. 15

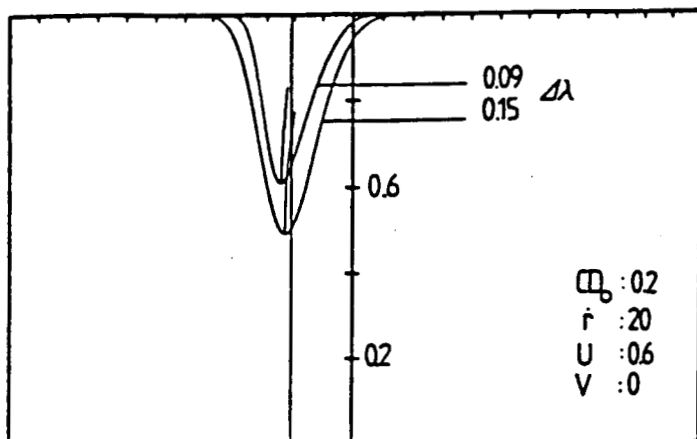


Fig. 16

$$R_2 - R_1 = \int_{t_1}^{t_2} v_{\text{atm}}(t) dt$$

Baade - Wesselink - radius :

$$R_{2\text{BW}} = (R_2 - R_1)_{v_{\text{atm}}} / (1 - R_1/R_2) = (R_2 - R_1)_{v_{\text{atm}}} / (1 - \theta_1/\theta_2)$$

$$\theta = 2R/r \quad \text{directly ?!}$$

$$\text{or from } \varphi_{\Delta} = (\theta^2/4) \phi_{\Delta} a_{\Delta}$$

$$\Delta \text{ bandpass or bolometric } \phi_{\text{bol}} \equiv \sigma_{\text{SB}} T_{\text{eff}}^4$$

ϕ_{Δ} : spectrum analysis

surface brightness method (Barnes, Evans)

Rayleigh-Jeans or infrared flux method (Blackwell, Shallis)

Baade - Wesselink - distance and -luminosity

$$r_{\text{BW}}^2 \varphi_{\Delta} = R_{\text{BW}}^2 \phi_{\Delta} a_{\Delta}$$

$$L_{\Delta\text{BW}} = 4\pi r_{\text{BW}}^2 \varphi_{\Delta} / a_{\Delta} = 4\pi R_{\text{BW}}^2 \phi_{\Delta}$$

Baade - Wesselink - mass

$$Q = P \sqrt{(M_{\text{BW}}/M_{\odot}) / (R_{\text{BW}}/R_{\odot})^3}$$